



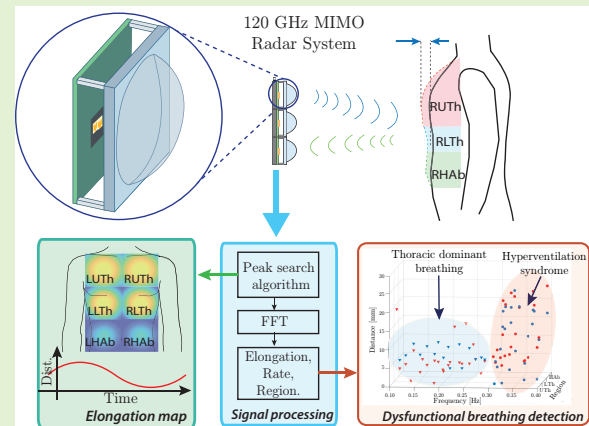


# In-Cabin MIMO Radar System for Human Dysfunctional Breathing Detection

María-José López , Student Member, IEEE, César Palacios , Student Member, IEEE, Jordi Romeu , Fellow, IEEE, and Luis Jofre-Roca , Life Fellow, IEEE

**Abstract**—The integration of wireless sensors into the automotive industry is making vehicles increasingly safe and autonomous. At present, vehicles are equipped with external sensors that facilitate maneuverability and braking and internal sensors that detect presence, seat belt state, and occupant vital signs. Early detection of dysfunctional breathing patterns can reduce the risk of accidents caused by drowsiness or fatigue. In this regard, this work presents a MIMO FMCW Radar System able to distinguish dysfunctional breathing patterns from human torso motion. The torso has been divided into six regions, and the amplitude of the elongation and the frequency of motion of each region have been measured during breathing. An elongation map is then constructed in order to graphically show the dysfunctional breathing patterns. The signal processing includes a peak search algorithm to detect elongation amplitude and a band pass frequency filter to minimize DC-component, random driver motion, and vehicle vibration. A torso elongation emulator phantom has been assembled with materials of skin-like relative permittivity and DC motors for calibration and validation of basic breathing patterns. Finally, the signal of the system is compared with that of a commercial respiration belt, and then the system is tested by performing measurements on people. The MIMO radar system is able to measure, differentiate, and classify patterns associated with dysfunctional breathing such as hyperventilation syndrome and thoracic dominant breathing.

**Index Terms**—FMCW radar; Dysfunctional breathing; In-Cabin; MIMO radar; Elongation map; mm-Waves; Breathing patterns.



## I. INTRODUCTION

In the last few years, vital sign monitoring inside of vehicles has attracted considerable interest of the scientific community, as well as the automotive industry, because it represents an important advance in the achievement of a secure autonomous vehicle [1], [2]. Furthermore, according to the Global Status Report on Road Safety, launched by the World Health Organization (WHO) in December 2018 [3], the eighth cause of death for people of all ages is road traffic accidents, reaching 1.35 million annual deaths. Additionally, the report shows that the four leading causes of death are ischemic heart disease, stroke, chronic obstructive pulmonary disease, and lower respiratory infections. Related research supports the notion that the number of traffic accidents can

be reduced by early detection of abnormal vital signs [4], [5]. Vital sign indicators basically include pulse, temperature, respiration rate, and blood pressure. The human breathing rate is most sensitive to changes in human health status and is a key indicator of adverse events like sleepiness, fatigue, or stress arising from long driving time [6].

In the area of vital sign monitoring research, many efforts have been made to accurately measure the breathing rate and heart beat. Some methods rely on wearable contact systems such as wristbands, chest straps, or compression garments [7]–[10]. Despite their high precision and ease of assembly, contact systems may cause discomfort to the subject due to continuous skin contact. Non-contact vital sign monitoring systems, by contrast, are a non-invasive technique pioneered by cameras [11], [12] and powered by recent advances in wireless sensors, e.g., radars. Regarding radar systems, it is possible to differentiate between systems tested in rooms or open spaces [13]–[17] and those tested inside a vehicle [18]–[20].

In this work, a new contactless method to monitor the functional breathing of a driver inside a vehicle is proposed. It is based on continuous selective scanning of six regions of the frontal torso using a 120 GHz FMCW MIMO Radar

This work was supported by the Spanish “Comision Interministerial de Ciencia y Tecnologia” (CICYT) under projects PID2019-107885GB-C31 and MDM2016-O6OO; Catalan Research Group 2017 SGR 219; and “Secretaría Nacional de Educación Superior, Ciencia, Tecnología e Innovación” (SENESCYT) from the Ecuadorian government.

M.J. López, C. Palacios, J. Romeu and L. Jofre-Roca are with the Dept. Signal Theory and Communications, Technical University of Catalonia, Barcelona 08034, Spain.

Corresponding author: M. J. López (email: maria.jose.lopez.montero@upc.edu).

System, making it possible to manufacture small-sized sensors with low energy consumption and non-intrusive placement in the vehicle. The proposed radar lensed arrangement may have higher effectiveness with comparable costs to the optical camera systems.

Within the framework of this work, the term "elongation mode" has been introduced to refer to both the amplitude of the elongation and the frequency of the motion of six torso regions during breathing in real-time [21]. The elongation mode measurements are used to produce an elongation map of the torso, able to visually show the breathing functional state of the person inside a vehicle. The elongation maps are then compared to dysfunctional breathing patterns related to the emotional and physiological state of the person, which can have a negative impact on driving, such as hyperventilation syndrome and thoracic dominant breathing, as classified in [22].

Furthermore, this work presents: (i) a novel radar-based method for detecting dysfunctional breathing patterns by means of elongation mode measurements of the front of the human torso of a driver; (ii) numerical simulations to establish the optimal pointing and focusing angles for six torso regions; (iii) measurements performed on a torso elongation emulator phantom based on DC-motors and dielectric characteristics of human skin; and (iv) real-time experiments for breathing rate detection and dysfunctional breathing classification. The paper has been organized as follows. First, an introduction is presented in section I. Section II, then provides a functional study of breathing, which includes a review of relevant related works as well as an examination of the operation of the In-Cabin MIMO Radar System. Next, an experimental demonstration of the system is provided in Section III. Finally, Section IV, summarizes the work and provides conclusions.

## II. THEORETICAL BACKGROUND AND SYSTEM DESCRIPTION

In order to establish the capabilities and limitations of the proposed system, an in-depth study on the emerging concept of dysfunctional breathing patterns is presented in this section. Then, the theoretical basis that supports the conversion of a physical magnitude to an electromagnetic signal and the processing of such a signal is also explained.

### A. Dysfunctional Breathing Study

During the respiratory process, the variation in lung volume and thoracic cross-section shows a linear correlation with displacement of the rib cage and abdomen, as measured through magnetic resonance imaging in [23]. In [24], the torso movements during deep and quiet breathing were studied by spirometry. The average respiratory rate was 14.0 and 7.4 breaths per minute, during quiet and deep breathing, respectively. In [25], authors found that there is less abdominal movement in females than in males, except in the supine position, and that the thoracic displacement is greater than the abdominal one during quiet and deep breathing in the sitting position. Measurements were done by means of a 3-dimensional motion capture system.

Numerous medical issues, such as potential injury or metabolic disorders, might cause the breathing rate (BR) to become irregular [26], [27]. Shallow, deep, rapid breathing patterns along with irregular movement of the torso can all be signs of dysfunctional breathing. Dysfunctional breathing is a term used to refer to disorders of breathing patterns that occur as a physiological response to a disease and can cause dyspnoea and other symptoms [28], [29]. Dyspnoea is an uncomfortable sensation of not being able to breathe properly [30]. According to [22], dysfunctional breathing can be classified into five different patterns:

- 1) Hyperventilation syndrome is excessive deep rapid breathing caused by anxiety, heart diseases, and lung pathologies [31]–[33].
- 2) Periodic deep sighs are breaths accompanied by an irregular respiratory pattern [34], [35].
- 3) Thoracic dominant breathing may be caused by some somatic diseases, or in the case of not relying on a disease that is considered dysfunctional and produces dyspnea. This type of breathing often occurs in patients with increasing ventilation [36], [37].
- 4) Forced abdominal breathing is accompanied by excessive abdominal muscle contraction [38], [39].
- 5) Thoraco-abdominal asynchrony occurs when there is a delay between the thoracic and abdominal contractions, which results in an ineffective breathing mechanism [40], [41].

### B. MIMO Radar system operation

The MIMO radar system is composed of three main stages: the radar signal conditioning, the received signal processing, and the generated real-time elongation map for dysfunctional breathing detection. Fig. 1 shows a block diagram of the system operation.

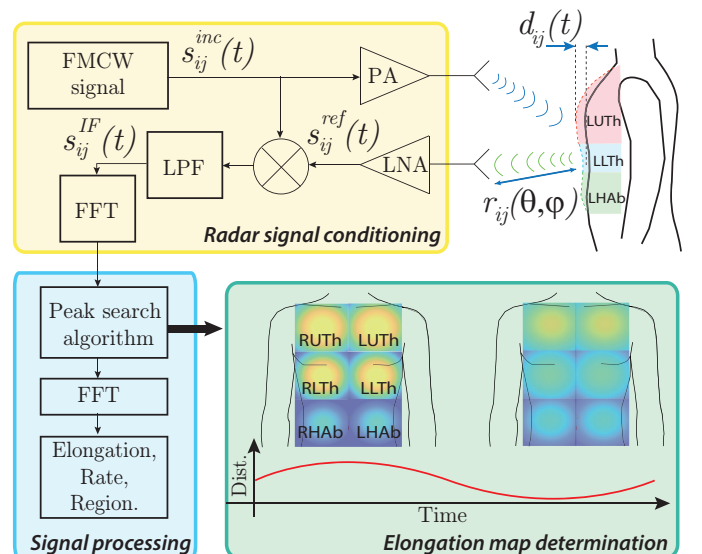


Fig. 1: MIMO radar system. The block diagram show the different phases of the system.

The incident  $s_{ij}^{inc}(t)$  and reflected  $s_{ij}^{ref}(t)$  radar signals are multiplied to obtain the intermediate frequency (IF) signal

$s_{ij}^{IF}(t)$  at 200 MHz. The variable  $r_{ij}(\theta, \phi)$  represents the initial position and  $d_{ij}(t)$  is the positive or negative displacement of each torso region during breathing with respect to the rest position, subscripts  $ij$  are used to identify each of the torso regions, as described in Section II-B.2.

1) **Radar signal conditioning:** In order to have a functional view of the state of the human torso generated by radar, six torso regions have been defined, as follows: First, a line is drawn from the center of the clavicles to the navel; then, a horizontal line is drawn at the fourth rib level for the left and right upper thoracic regions (LTh, RTh); next, another line at the ninth rib level defines the left and right lower thoracic regions (LLTh, RLTh); and finally, a third line at the level of the navel is traced for the left and right half abdominal regions (LHAb, RHAb). Figure 1 shows the acronyms of each of the regions. The right and left sides have been defined from the radar point of view.

The elongation modes of each region have been measured with a FMCW radar (Silicon Radar, Co., Germany) that operates at 120 GHz with a maximum bandwidth of 6 GHz and adjustable maximum range of 10 m with a noise figure of 8.7 dB. The proposed system is composed of six radars mounted in an arrangement of  $2 \times 3$ , each one of them targeting one of the six torso regions.

Dielectric lenses (Silicon Radar, Co., Germany) have been placed in front of the transmitter and receiver antennas to increase its directivity. The antenna-lens arrangement has been analyzed according to two approaches: (i) six single-radar with single-lens arrangements, and (ii) a single-lens with a six-radar arrangement. The first method occupies an approximate area of  $8 \text{ cm} \times 12 \text{ cm}$  in a  $3 \times 2$  arrangement. Fig. 2a presents the geometry of a single radar with a single lens. In the second approach, the six pairs of antennas have been placed behind a single lens, occupying an area of  $3.6 \text{ cm} \times 3.6 \text{ cm}$ , thus allowing the lens to be placed, e.g., in the lower left corner of the rearview mirror of the vehicle, as sketched in Fig. 2b.

The individual dielectric lens is made of polytetrafluoroethylene (PTFE),  $\epsilon_r^* = 2.05 + j(5.53 \times 10^{-4})$  [42]. The diameter of the lens is  $l_{len} = 31.8 \text{ mm}$ , the thickness is  $h_{len} = 15.7 \text{ mm}$ , and it has been placed at a distance  $p_{len} = 15.0 \text{ mm}$  away from the antennas. The single encapsulated microchip containing the antennas has an area of  $0.64 \text{ cm}^2$  with  $\lambda \approx 0.25 \text{ cm}$ .

The far-field radiation patterns of the lenses have been simulated by using comprehensive electromagnetic simulation software, FEKO, in order to analyze the half-power beam width (HPBW). The simulated HPBW of a single radar without lens is  $46.80^\circ$  and with lens it reduces to  $6.40^\circ$ , as shown in Fig. 3.

As a first approach, when the rear-view mirror is manually adjusted, the directional pointing of the radar adjustment is done as well. The relative signal levels of each radar can be compared to assess if the torso is correctly pointed. To optimally illuminate each torso region, the vector normal to the radar plane points to the ‘‘Xiphoid process’’ bone [43]. After this global adjustment, each antenna behind the lens has been moved transversely and longitudinally until the beam reaches the corresponding region with a scanning ratio of a

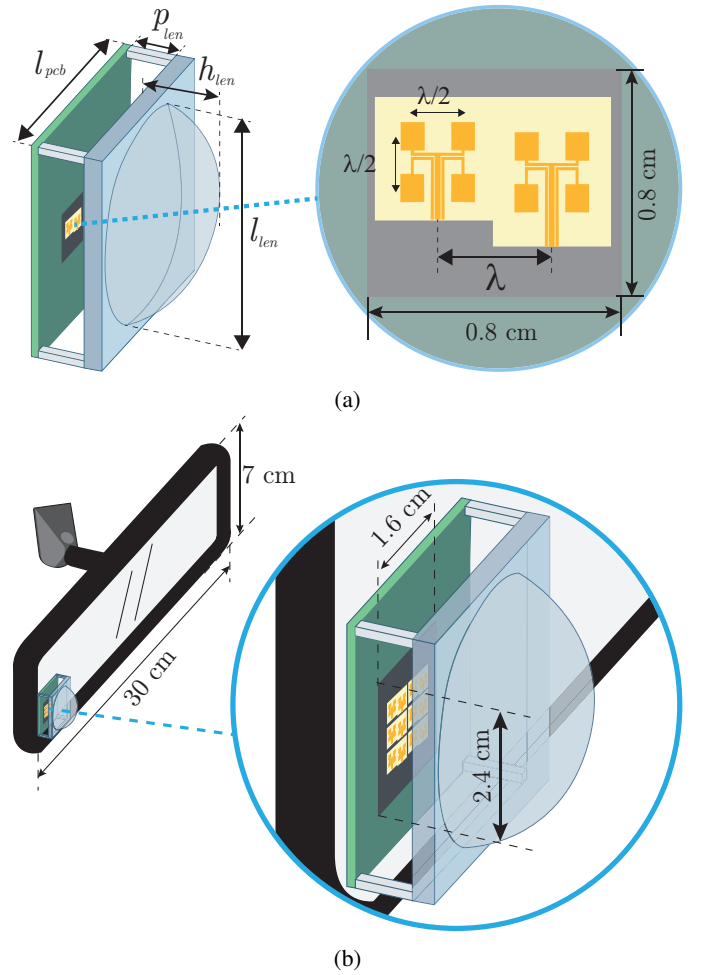


Fig. 2: (a) On the left hand is shown an individual radar and its respective lens (approach i); on the right hand is the geometry of the transmitting and receiving antenna. (b) Six radars hidden behind a single dielectric lens (approach ii), with a sketch of their location in the rearview mirror.

$-3 \text{ dB}$  beamwidth per each  $\lambda/2$  displacement. The variation in the reflective index in the path between the radar and the skin due to the multilayer clothing or eventual objects stored over the thorax, such as in a pocket, has been estimated to be around  $2\text{-}4 \text{ dB}$  in the amplitude of the received signal that may be assumed by the existing radar dynamic range. Eventual reflections towards a different radar may be neglected by the sequential scanning operation of the six-radar system arrangement.

The radar spot is reconstructed from the simulated HPBW for the E- and H-planes of each radar. Table I shows the HPBW of each radar along with the minor and major radius of the ellipse illuminating the respective chest region.

2) **Received signal processing:** In a FMCW radar, the incident chirp  $s_{ij}^{inc}$ , as shown in (1), is a sinusoidal signal with a carrier frequency  $f_c$ , a bandwidth  $BW$ , and a period  $T_s$  that is linearly swept in the range  $f_c \pm BW/2$  with a positive slope  $BW/T_s$ . In all the formulation subscripts  $ij$  has been used to identify each of the regions, where  $i = \{1, 2, 3\}$  indicates the upper, lower, and abdominal regions and  $j = \{1, 2\}$  indicates

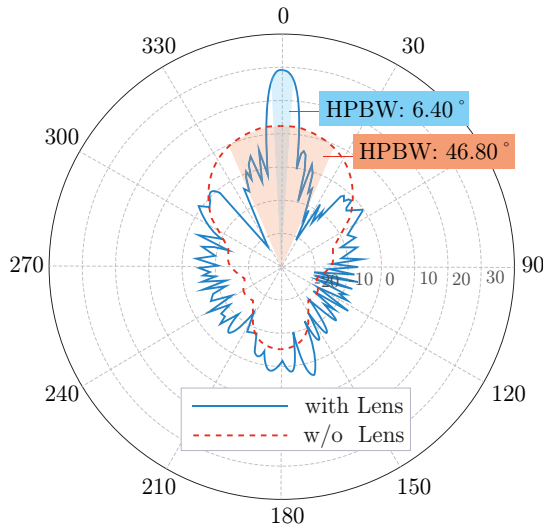


Fig. 3: Radiation pattern of one radar antenna from the six single-radar with single-lens arrangement with the lens (blue solid line) and without a lens (red dashed line), placed at a distance  $p_{len}$ .

Region	HPBW H-Plane ( $^\circ$ )	HPBW E-Plane ( $^\circ$ )	Minor axis (cm)	Major axis (cm)
LUTh	5.42	5.86	6.75	6.23
RUTh	6.54	5.83	6.72	7.34
LLTh	6.37	5.92	6.73	7.21
RLTh	7.44	5.92	6.72	8.43
LA	11.84	6.17	6.92	13.41
RA	11.55	6.13	6.94	13.44

TABLE I: Simulated HPBW and spot size.

the left and right side of the torso, respectively.

$$s_{ij}^{inc}(t) = A_t \exp(j(2\pi f_c t + \pi \frac{BW}{T_s} t^2 + \Phi_{ij}^{inc}(t))), \quad (1)$$

where,  $A_t$  represents the transmitted signal amplitude,  $\Phi_{ij}^{inc}$  is the initial phase, and  $t$  is the measuring time. The positive or negative displacement  $d_{ij}(t)$  of each region during breathing, causes a delay  $t_{ij}^{del} = \frac{2(r_{ij}(\theta, \phi) + d_{ij}(t))}{c}$  on the transmitted signal, where  $r_{ij}(\theta, \phi)$  is the initial position of each region, and the factor of 2 represents the round-trip time of the radar reflected wave. Thus, the received signal  $S_{ij}^{ref}$  is

$$s_{ij}^{ref}(t) = A_r \exp(j(2\pi f_c(t - t_{ij}^{del}) + \pi \frac{BW}{T_s}(t - t_{ij}^{del})^2 + \Phi_{ij}^{inc}(t - t_{ij}^{del}))) \quad (2)$$

The beat signal is the product of  $s_{ij}^{inc}(t)$  and  $s_{ij}^{ref}(t)$  passed through a low-pass filter (LPF). The intermediate frequency (IF) at the output of the LPF, can be directly written according to [44]–[48], as:

$$s_{ij}^{IF}(t) = A \exp(j(4\pi \frac{BW}{T_s} \frac{r_{ij}(\theta, \phi, t)}{c} t + \Phi_{ij}(t))) \quad (3)$$

where,

$$\Phi_{ij}(t) = 4\pi \frac{r_{ij}(\theta, \phi, t)}{\lambda} \quad (4)$$

represents the phase change caused by torso motion.

The frequency spectrum of (3) is obtained by implementing the Fast Fourier Transform (FFT). The frequency value with maximum power determines the instantaneous elongation of each single region. These FFT ranges are aggregated in a slow-span time matrix in order to have a spectrogram. The variation of the torso elongation amplitude is proportional to the change in phase that arrives at the receiving antenna. A peak search algorithm [49] enables obtaining the maximum elongation of every single region by examining the effect of changes in the width and height of peaks over time. The envelope of the output after the peak search algorithm contains the breathing rate signal, heart beat information, random person movements, car vibration, and a DC component. Normal and dysfunctional breathing patterns can range from 0.2 to  $\approx 0.4$  Hz, whereas the normal and dysfunctional heart rate can be in the range of 1 Hz to even more than 2 Hz. Random movements in the driver (e.g., passing an arm in front of the chest, bending down, or turning the body) occur at very low frequencies, less than 0.1 Hz. Therefore, in order to contain the breathing and heart information, a bandpass filter with cut-off frequencies of 0.1 and 2 Hz has been implemented by using a cascading high-pass filter with a low-pass filter based on the biquadratic approach. Filtering also allows to eliminate the DC-component and to reduce noise in the frequency bandwidth. The stop-band attenuation of the filters is 60 dB and has been implemented by software using Matlab.

3) *Elongation maps determination*: By processing individually the information of each of the 6 regions, it is possible to construct a map of torso elongation that allows to visually control the displacement of each region over time. Elongation maps are constructed by superimposing a surface plot with elongation measurements over a torso diagram. In a real system running inside a car, this elongation map would be presented on a screen along with measured data, statistics, and possible alerts to the driver. Figure 4 shows the temporal sequence of three instantaneous elongation maps for abdominal breathing.

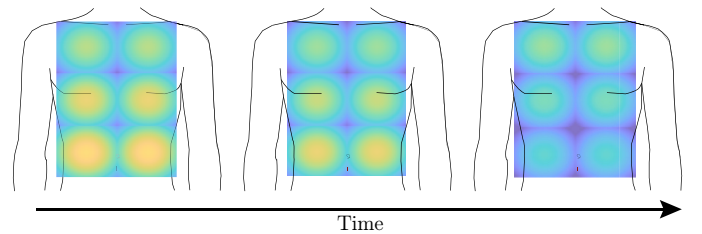


Fig. 4: Real-time captured elongation maps.

The elongation amplitude and movement frequency information associated with each of the regions are classified according to hyperventilation syndrome and thoraco-abdominal asynchrony by statistical analysis.

### III. EXPERIMENTAL RESULTS

The feasibility of the system was analyzed through several experiments and statistical studies of the results. This experimental section is structured as follows: (i) Calibration and

sensitivity measurements using a torso elongation emulator phantom, (ii) real-time breathing measurements on people, and (iii) detection and classification of dysfunctional breathing.

### A. Torso elongation emulator phantom

A phantom of the torso was manufactured to emulate the elongation amplitude and frequency of six torso region movements. The phantom was used to calibrate the radars and measure the system sensitivity, leaving out the effect of vibrations and random movement of the human body. The mechanical part is composed of six DC motors, whose travel and speed are regulated via a programmable microcontroller. At the moving end of each DC motor, a square-shaped piece of plasticized PVC with relative permittivity similar to that of human skin at 120 GHz ( $5.60 - j7.09$ ) [50] has been placed. Radars are located 65 cm from the phantom, with each radar pointing to the corresponding region. The pointing angles of each radar are achieved by varying the position of the antennas behind the lenses using a two-axis millimetric positioner. In Fig. 5, a graphical representation of the emulator phantom is presented.

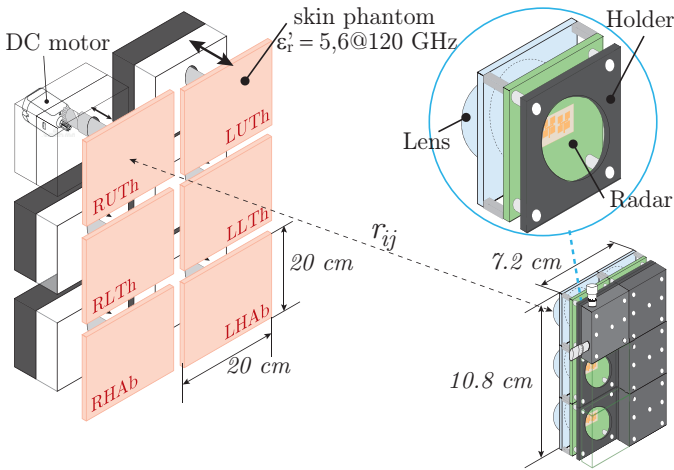


Fig. 5: Torso elongation emulator phantom.

The variation in amplitude elongation and frequency rate has been measured for four basic breathing patterns that are not associated with any specific region of the torso, such as those of dysfunctional breathing. These patterns are: Eupnea at 12 breath per minute (bpm), Tachypnea at 23 bpm, Bradypnea at 7 bpm, and Hypernea that is deep breath at 12 bpm, generated by the torso elongation emulator phantom. The instantaneous elongation amplitude is stored in an array over time to create a spectrogram of the elongation, and the peak search algorithm enables plotting the elongation amplitude variation over time. A sinusoidal curve fitting has been drawn together with measured breathing signal of each basic pattern, as depicted in Fig. 6. The torso elongation emulator phantom allowed determining the sensitivity of the system from the minimum step of the DC motor, which is 0.1 mm. The calibration was done taking into account the maximum radar range of 3.0 m over  $N = 1024$  that are the samples used for the FFT.

In order to calculate the sensitivity of the system the radar cross section (RCS) of a single region has been calculated at

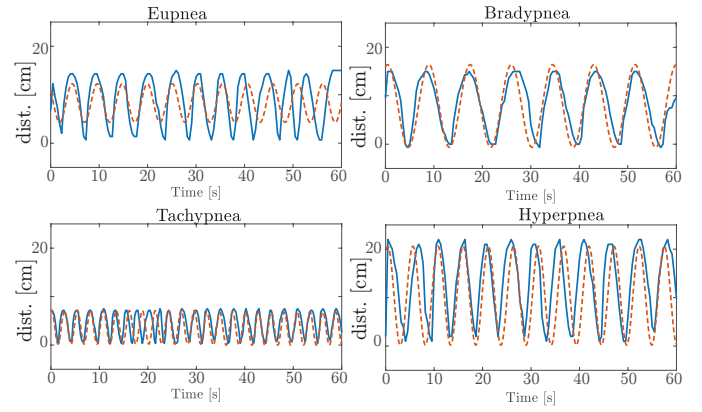


Fig. 6: 'Emulated breathing patterns' In blue, the signal from the emulator phantom, and in red, a software-generated signal.

a distance of 65 cm. At a frequency of 120 GHz the RCS of a flat plasticized PVC surface of  $10 \text{ cm} \times 10 \text{ cm}$  is  $\sigma_{max} = 35 \text{ dBsm}$ . To calculate the signal-to-noise ratio (SNR) several simulations of the elongation variation were performed, then the average value  $\bar{s}$  and variance  $\sigma^2$  was extracted to apply  $SNR = |\bar{s}|^2 / \sigma^2$ . For a set of 1000 measurements and without averaging, the calculated SNR is 15.2 dB. The limited SNR of the system can cause error in the measured elongation. The Cramér-Rao lower bound for range error variance due to SNR can be calculated as

$$\text{var}(R) \geq \frac{\lambda^2}{4\pi^2 N (SNR)} \quad (5)$$

If  $N = 1024$  samples and  $SNR = 15.2 \text{ dB}$ , the standard error of range has a bound of  $4.6 \mu\text{m}$ . Adding the system imperfections as in [51], the range error can be in the order of  $50 \mu\text{m}$ , which is one order of magnitude less than the amplitude of elongation measured.

### B. Real-time breathing measurements

Prior to the detection of dysfunctional patterns, experiments have been carried out to measure cardiac and respiratory rhythms of an individual subject. The test subject was a 33-year-old adult male who was in good health and had no history of previous respiratory conditions. He signed an informed consent form, where the information about the measurement protocol and the study objectives were provided.

The subject was seated at a distance of 65.0 cm with the radars pointing at the level of the Xiphoid process, as presented in Fig. 7a. Then, it was instructed to simulate deep and shallow breaths without taking into account the respiratory rhythm. The measured signal of each radar was compared to the signal of a commercial breathing measuring belt (Vernier, Germany) that measures the respiration effort and respiration rate from the force [N] exerted on the strap by the chest during breathing, with a resolution of 0.01 N, and a response time of 50.0 ms.

The breathing signal was always observed at the expected rate compared to the belt signal. The measured time and frequency-domain signals of a single radar and belt are plotted in Fig. 7b and Fig. 7c, respectively. The measured frequency is 0.24 Hz, that correspond to 14.4bpm, for both radar and belt

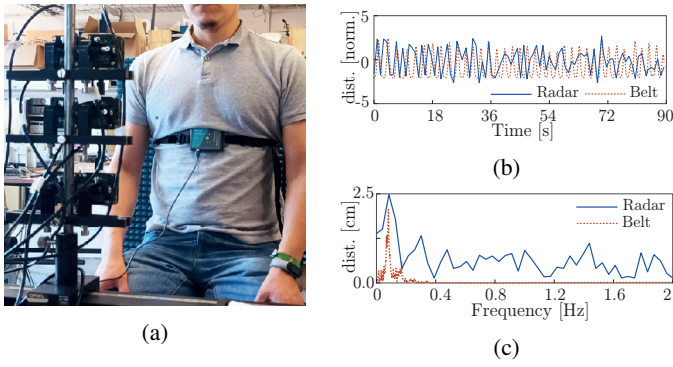


Fig. 7: a) Breathing rate measurement set-up, b) Measured elongation amplitude, and c) FFT of the belt and radar signals. (Radar signal - blue solid line, Belt signal - red dashed line).

and the maximum measured elongation was  $\approx 2.5$  cm. The magnitude of the force measured with the belt has been drawn versus the instantaneous elongation measured with the radar, both signals show a positive correlation, as plotted in Fig. 8.

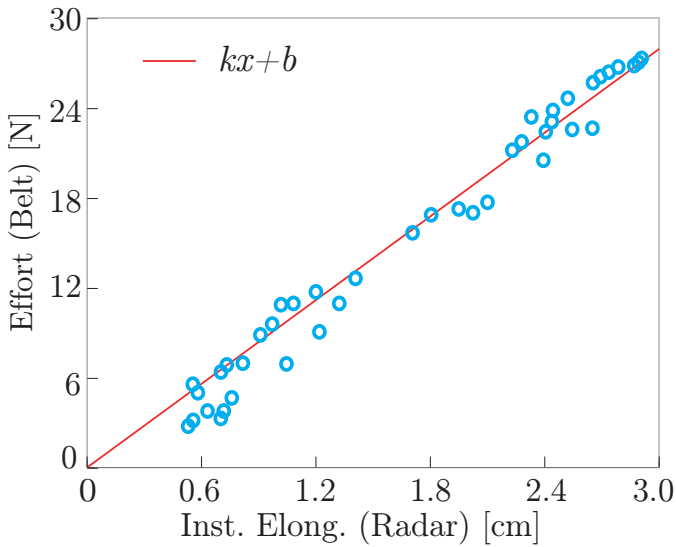


Fig. 8: Measured Effort from belt and instantaneous elongation from radar, of a person performing a normal deep abdominal breathing pattern. The trend shows a positive linear relation with  $k = 9.3$  and  $b = 0$ .

### C. Detection and classification of dysfunctional breathing

The elongation amplitude and frequency measurements associated with each region analyzed over time allow the identification of patterns in which the dysfunctionality of the breathing process can be evidenced. Experiments to detect the type of dysfunctional breathing pattern involved a volunteer who was asked to act out hyperventilation syndrome and thoracic dominant breathing several times in one day, letting the MIMO radar system measure, classify, and show the resulting one.

1) *Thoracic dominant breathing*: The movement occurs at the thoracic region. Results show that during this pattern the upper and lower thoracic region move around  $20.0 \pm 0.5$  mm and abdominal  $10.0 \pm 0.1$  mm at an average frequency of 0.25 Hz.

2) *Hyperventilation syndrome*: The greatest movement occurs in the abdomen. The measured elongation in the upper and lower thoracic region move  $10.0 \pm 0.1$  mm and abdominal  $30.0 \pm 0.5$  mm at an average frequency of 0.33 Hz.

3) *Heartbeat detection*: When breathing is thoracic, a new frequency component is evident at  $\approx 1.2$  Hz due to heartbeat, mainly in the LUTh and LLTh regions. When breathing is abdominal, although the range of elongation in RHAb and LHAb is greater than in the other four regions, the cardiac rhythm is slightly more difficult to detect, as presented in Fig. 9.

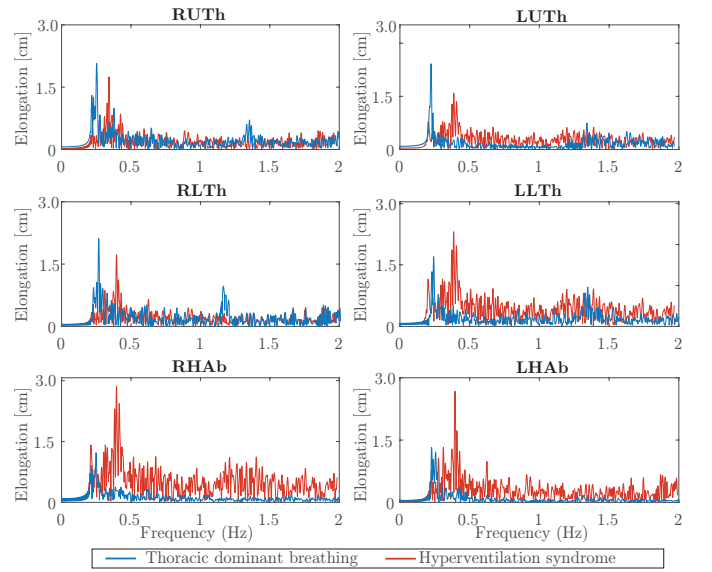


Fig. 9: Frequency response of the six torso regions during thoracic dominant breathing (blue-color) and hyperventilation syndrome (red-color).

The collected data from the two patterns has been plotted in Fig. 10 using a 3-coordinate axis that relates each of the regions to elongation and frequency. The dysfunctional breathing patterns analysed in this study can be correctly distinguished in 98% of the measurements. If the breathing is thoracic dominant, the heart beat is detected in the 81% of the measurements and can be seen in the LUTh and LLTh regions, mainly. When hyperventilation syndrome is occurring, the heart beat is detected in 60% of measurements.

## IV. CONCLUSIONS AND FUTURE WORK

A new method for monitoring the physiological breathing status of a person inside a vehicle has been presented. The method is based on a MIMO radar dysfunctional breathing detection of the elongation maps of the human torso. The results show the feasibility of using the system for the differentiation and classification of hyperventilation syndrome and thoracic dominant breathing, with results consistent with data available in the literature.

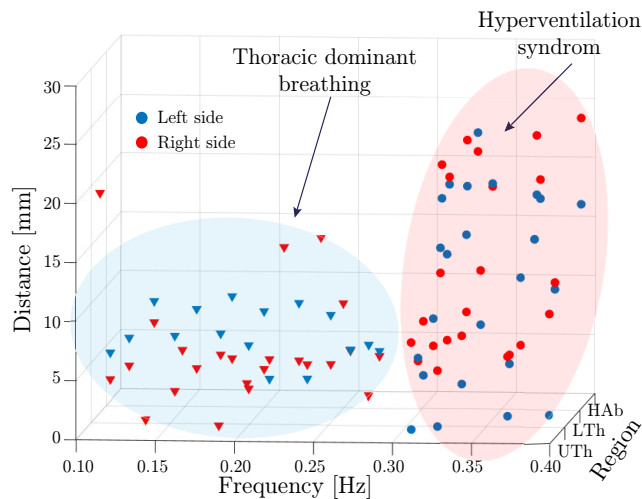


Fig. 10: Dysfunctional breathing detection. The triangles correspond to the number of experiments performed for thoracic dominant breathing and the circles for hyperventilation syndrome. Blue and red colors has been used to distinguish left and right side of the torso, respectively.

The proposed six-radar system increases the robustness of the acquired information and allows the determination of dysfunctional patterns that depend on the heart rhythm and paradoxical movements (asynchronous movement between chest and abdomen) in the thorax, as in the case of the thoracic dominant breathing pattern. The consideration of just three regions would make it possible to distinguish between the hyperventilation syndrome and dominant thoracic respiration, but the division of the torso into left and right sides creating a six regions topology enables the addition of the cardiac rhythm as a criterion of classification, increasing the possibility and reliability of the system to diagnose the state of the person.

The fact that the radars operate at millimeter waves means small antennas and devices that do not cause distraction or interfere with the vehicle's operation. The system can be used preventively so that the driver of the vehicle can be alerted in a timely manner about changes in breathing patterns caused by anxiety, stress, tiredness, etc. that cause dysfunctional breathing.

The viability of the six-radar system has been determined through testing with a single volunteer; however, future research will include more participants in a sitting position, in order to draw general conclusions from measurements that are not subject-specific. The data processing can be extended by adding artificial intelligence algorithms, increasing the number of dysfunctional patterns detected, and taking detection a step further by providing passenger feedback capable of influencing their emotional and physiological status.

#### ACKNOWLEDGEMENTS

This work was supported by the Spanish "Comision Interministerial de Ciencia y Tecnologia" (CICYT) under projects PID2019-107885GB-C31 and MDM2016-O600; Catalan Research Group 2017 SGR 219; and "Secretaría Nacional

de Educación Superior, Ciencia, Tecnología e Innovación" (SENESCYT) from the Ecuadorian government.

#### REFERENCES

- [1] P. Mallozzi, P. Pelliccione, A. Knauss, C. Berger, and N. Mohammadiha, *Autonomous Vehicles: State of the Art, Future Trends, and Challenges*. Cham: Springer International Publishing, 2019, pp. 347–367. [Online]. Available: <https://doi.org/10.1007/978-3-030-12157-0-16>
- [2] J. W. Koon, "Ai-based machine vision & the future of automotive in-cabin technologies," *Tech Briefs*, vol. 44, no. 5, 2020.
- [3] W. H. Organization et al., "Global status report on road safety 2018: summary," World Health Organization, Tech. Rep., 2018.
- [4] M. Shu, M. Tang, M. Yang, and N. Wei, "The vital signs real-time monitoring system based on internet of things," in *2017 4th International Conference on Information Science and Control Engineering (ICISCE)*. IEEE, 2017, pp. 747–751.
- [5] V. Melcher, F. Diederichs, R. Maestre, C. Hofmann, J.-M. Nacenta, J. van Gent, D. Kusić, and B. Žagar, "Smart vital signs and accident monitoring system for motorcyclists embedded in helmets and garments for advanced ecall emergency assistance and health analysis monitoring," *Procedia Manufacturing*, vol. 3, pp. 3208–3213, 2015.
- [6] M. A. Cretikos, R. Bellomo, K. Hillman, J. Chen, S. Finfer, and A. Flabouris, "Respiratory rate: the neglected vital sign," *Medical Journal of Australia*, vol. 188, no. 11, pp. 657–659, 2008.
- [7] G. Tomich, D. França, A. Diório, R. Britto, R. Sampaio, and V. Parreira, "Breathing pattern, thoracoabdominal motion and muscular activity during three breathing exercises," *Brazilian Journal of Medical and Biological Research*, vol. 40, no. 10, pp. 1409–1417, 2007.
- [8] V. F. Parreira, C. J. Bueno, D. C. França, D. S. Vieira, D. R. Pereira, and R. R. Britto, "Breathing pattern and thoracoabdominal motion in healthy individuals: influence of age and sex," *Brazilian Journal of Physical Therapy*, vol. 14, pp. 411–416, 2010.
- [9] M. Weenk, H. van Goor, B. Frietman, L. J. Engelen, C. J. van Laarhoven, J. Smit, S. J. Bredie, and T. H. van de Belt, "Continuous monitoring of vital signs using wearable devices on the general ward: pilot study," *JMIR mHealth and uHealth*, vol. 5, no. 7, p. e91, 2017.
- [10] A. M. Chan, N. Selvaraj, N. Ferdosi, and R. Narasimhan, "Wireless patch sensor for remote monitoring of heart rate, respiration, activity, and falls," in *2013 35th Annual international conference of the IEEE engineering in medicine and biology society (EMBC)*. IEEE, 2013, pp. 6115–6118.
- [11] C. Romano, E. Schena, S. Silvestri, and C. Massaroni, "Non-contact respiratory monitoring using an rgb camera for real-world applications," *Sensors*, vol. 21, no. 15, p. 5126, 2021.
- [12] Y.-C. Lee, A. Syakura, M. A. Khalil, C.-H. Wu, Y.-F. Ding, and C.-W. Wang, "A real-time camera-based adaptive breathing monitoring system," *Medical & Biological Engineering & Computing*, vol. 59, no. 6, pp. 1285–1298, 2021.
- [13] A. Prat, S. Blanch, A. Aguiasca, J. Romeu, and A. Broquetas, "Collimated beam fmcw radar for vital sign patient monitoring," *IEEE Transactions on Antennas and Propagation*, vol. 67, no. 8, pp. 5073–5080, 2018.
- [14] K. Yamamoto, K. Toyoda, and T. Ohtsuki, "Cnn-based respiration rate estimation in indoor environments via mimo fmcw radar," in *2019 IEEE Global Communications Conference (GLOBECOM)*. IEEE, 2019, pp. 1–6.
- [15] M. Sidikova, R. Martinek, A. Kawala-Sterniuk, M. Ladrova, R. Jaros, L. Danys, and P. Simonik, "Vital sign monitoring in car seats based on electrocardiography, ballistocardiography and seismocardiography: A review," *Sensors*, vol. 20, no. 19, p. 5699, 2020.
- [16] E. Turppa, J. M. Kortelainen, O. Antropov, and T. Kiuru, "Vital sign monitoring using fmcw radar in various sleeping scenarios," *Sensors*, vol. 20, no. 22, p. 6505, 2020.
- [17] M. Alizadeh, G. Shaker, J. C. M. De Almeida, P. P. Morita, and S. Safavi-Naeini, "Remote monitoring of human vital signs using mm-wave fmcw radar," *IEEE Access*, vol. 7, pp. 54958–54968, 2019.
- [18] I. Nejadgholi, H. Sadreazami, Z. Baird, S. Rajan, and M. Bolic, "Estimation of breathing rate with confidence interval using single-channel cw radar," *Journal of healthcare engineering*, vol. 2019, 2019.
- [19] K. Van Loon, M. Breteler, L. Van Wolfwinkel, A. R. Leyssius, S. Kossen, C. Kalkman, B. van Zaane, and L. Peelen, "Wireless non-invasive continuous respiratory monitoring with fmcw radar: a clinical validation study," *Journal of clinical monitoring and computing*, vol. 30, no. 6, pp. 797–805, 2016.

- [20] A. Lazaro, M. Lazaro, R. Villarino, and D. Girbau, "Seat-occupancy detection system and breathing rate monitoring based on a low-cost mm-wave radar at 60 ghz," *IEEE Access*, vol. 9, pp. 115 403–115 414, 2021.
- [21] M. J. López Montero, A. Aguasca Solé, J. Romeu Robert, and L. Jofre Roca, "In-cabin 120 ghz radar system for functional human breathing monitoring in a 3d scenario," in *XXXVI Simposium Nacional de la Unión Científica Internacional de Radio (URSI 2021 Vigo): virtual: Septiembre 20-24, 2021: actas*. Iñigo Cuiñas Gómez, 2021.
- [22] R. Boulding, R. Stacey, R. Niven, and S. J. Fowler, "Dysfunctional breathing: a review of the literature and proposal for classification," *European Respiratory Review*, vol. 25, no. 141, pp. 287–294, 2016.
- [23] T. Kondo, I. Kobayashi, Y. Taguchi, Y. Ohta, and N. Yanagimachi, "A dynamic analysis of chest wall motions with mri in healthy young subjects \*," *Respirology*, vol. 5, no. 1, pp. 19–25, 2000. [Online]. Available: <https://onlinelibrary.wiley.com/doi/abs/10.1046/j.1440-1843.2000.00221.x>
- [24] M. Ragnarsdóttir and E. K. Kristinsdóttir, "Breathing movements and breathing patterns among healthy men and women 20–69 years of age," *Respiration*, vol. 73, no. 1, pp. 48–54, 2006.
- [25] H. Kaneko and J. Horie, "Breathing movements of the chest and abdominal wall in healthy subjects," *Respiratory care*, vol. 57, no. 9, pp. 1442–1451, 2012.
- [26] C. W. Baffi, L. Wood, D. Winnica, P. J. Strollo Jr, M. T. Gladwin, L. G. Que, and F. Holguin, "Metabolic syndrome and the lung," *Chest*, vol. 149, no. 6, pp. 1525–1534, 2016.
- [27] L. Whited and D. D. Graham, "Abnormal respirations," in *StatPearls [Internet]*. StatPearls Publishing, 2021.
- [28] L. Laviolette and P. Laveneziana, "Dyspnoea: a multidimensional and multidisciplinary approach," *European Respiratory Journal*, vol. 43, no. 6, pp. 1750–1762, 2014.
- [29] A. AC03314944, *Pathophysiology of haemostasis and thrombosis*. Karger, 2002.
- [30] M. J. Tobin, "Dyspnea," *Archives of Internal Medicine*, vol. 150, no. 8, pp. 1604–1613, 08 1990. [Online]. Available: <https://doi.org/10.1001/archinte.1990.00040031604007>
- [31] H. Folgering, "The pathophysiology of hyperventilation syndrome." *Monaldi archives for chest disease= Archivio Monaldi per le malattie del torace*, vol. 54, no. 4, pp. 365–372, 1999.
- [32] W. N. Gardner, "The pathophysiology of hyperventilation disorders," *Chest*, vol. 109, no. 2, pp. 516–534, 1996.
- [33] M. Thomas, R. K. McKinley, E. Freeman, and C. Foy, "Prevalence of dysfunctional breathing in patients treated for asthma in primary care: cross sectional survey," *Bmj*, vol. 322, no. 7294, pp. 1098–1100, 2001.
- [34] M. J. Tobin, T. S. Chadha, G. Jenouri, S. J. Birch, H. B. Gazeroglu, and M. A. Sackner, "Breathing patterns: 2. diseased subjects," *Chest*, vol. 84, no. 3, pp. 286–294, 1983.
- [35] C. O. Prys-Picard, F. Kellett, and R. M. Niven, "Disproportionate breathlessness associated with deep sighing breathing in a patient presenting with difficult-to-treat asthma," *Chest*, vol. 130, no. 6, pp. 1723–1725, 2006.
- [36] K. J. Killian and N. L. Jones, "Respiratory muscles and dyspnea." *Clinics in chest medicine*, vol. 9, no. 2, pp. 237–248, 1988.
- [37] R. Courtney, J. Van Dixhoorn, K. M. Greenwood, and E. L. Anthonissen, "Medically unexplained dyspnea: partly moderated by dysfunctional (thoracic dominant) breathing pattern," *Journal of Asthma*, vol. 48, no. 3, pp. 259–265, 2011.
- [38] R. Bianchi, F. Gigliotti, I. Romagnoli, B. Lanini, C. Castellani, M. Grazzini, and G. Scano, "Chest wall kinematics and breathlessness during pursed-lip breathing in patients with copd," *Chest*, vol. 125, no. 2, pp. 459–465, 2004.
- [39] M. Gorini, G. Misuri, R. Duranti, I. Iandelli, M. Mancini, and G. Scano, "Abdominal muscle recruitment and peepi during bronchoconstriction in chronic obstructive pulmonary disease." *Thorax*, vol. 52, no. 4, pp. 355–361, 1997.
- [40] J. Upton, D. Brodie, D. Beales, J. Richardson, S. Jack, C. Warburton, M. Thomas, and A. Kendrick, "Correlation between perceived asthma control and thoraco-abdominal asynchrony in primary care patients diagnosed with asthma," *Journal of Asthma*, vol. 49, no. 8, pp. 822–829, 2012.
- [41] J.-Y. Chien, S.-Y. Ruan, Y.-C. T. Huang, C.-J. Yu, and P.-C. Yang, "Asynchronous thoraco-abdominal motion contributes to decreased 6-minute walk test in patients with copd," *Respiratory Care*, vol. 58, no. 2, pp. 320–326, 2013.
- [42] T. Shimizu, Y. Kawahara, S. Akasaka, and Y. Kogami, "Complex permittivity measurements of a ptfе substrate in w band by the cut-off circular waveguide method," in *2011 China-Japan Joint Microwave Conference*. IEEE, 2011, pp. 1–4.
- [43] J. E. Muscolino, *The muscle and bone palpation manual with trigger points, referral patterns and stretching*. Elsevier Health Sciences, 2008.
- [44] A. Anghel, G. Vasile, R. Cacoveanu, C. Ioana, and S. Ciocchina, "Short-range wideband fmcw radar for millimetric displacement measurements," *IEEE Transactions on Geoscience and Remote Sensing*, vol. 52, no. 9, pp. 5633–5642, 2014.
- [45] M. He, Y. Nian, and Y. Gong, "Novel signal processing method for vital sign monitoring using fmcw radar," *Biomedical Signal Processing and Control*, vol. 33, pp. 335–345, 2017.
- [46] L. Anitori, A. de Jong, and F. Nennie, "Fmcw radar for life-sign detection," in *2009 IEEE Radar Conference*. IEEE, 2009, pp. 1–6.
- [47] H. Lee, B.-H. Kim, J.-K. Park, S. W. Kim, and J.-G. Yook, "A resolution enhancement technique for remote monitoring of the vital signs of multiple subjects using a 24 ghz bandwidth-limited fmcw radar," *IEEE Access*, vol. 8, pp. 1240–1248, 2019.
- [48] G. Wang, J.-M. Munoz-Ferreras, C. Gu, C. Li, and R. Gomez-Garcia, "Application of linear-frequency-modulated continuous-wave (lfmcw) radars for tracking of vital signs," *IEEE transactions on microwave theory and techniques*, vol. 62, no. 6, pp. 1387–1399, 2014.
- [49] P. Du, W. A. Kibbe, and S. M. Lin, "Improved peak detection in mass spectrum by incorporating continuous wavelet transform-based pattern matching," *Bioinformatics*, vol. 22, no. 17, pp. 2059–2065, 07 2006. [Online]. Available: <https://doi.org/10.1093/bioinformatics/btl355>
- [50] T. Wu, T. S. Rappaport, and C. M. Collins, "The human body and millimeter-wave wireless communication systems: Interactions and implications," in *2015 IEEE International Conference on Communications (ICC)*. IEEE, 2015, pp. 2423–2429.
- [51] S. Scherr, S. Ayhan, B. Fischbach, A. Bhutani, M. Pauli, and T. Zwick, "An efficient frequency and phase estimation algorithm with crb performance for fmcw radar applications," *IEEE Transactions on Instrumentation and Measurement*, vol. 64, no. 7, pp. 1868–1875, 2014.



**María-José López** Ph. D. Candidate, (IEEE Student member, 2018). She received the Electronic engineering in telecommunications and networks degree in 2013 from the Escuela Superior Politécnica de Chimborazo (Riobamba, Ecuador), and the M.S. degree in Telecommunications Engineering from the University of Calabria (Cosenza, Italy) in 2017. She has held positions at Escuela Superior Politecnica de Chimborazo (2013-17), and belonged to the research group of the engineering faculty. In 2019 she received a scholarship from the Ecuadorian government to pursue postgraduate studies. She is currently working in the Signal Theory and Communications (TSC) Department, within the research group CommSensLab, UPC. Her research interests are focused on the use of radars for 5G applications related to human health and well-being.



**César Palacios** Ph. D. Candidate, (IEEE Student member, 2018). He received the B.S. degree in Telecommunication and Electronics Engineering in 2013 from the Private Technical University of Loja UTPL (Loja, Ecuador), and the M.S. degree in Electronics Engineering from the University of Calabria (Cosenza, Italy) in 2017. He is currently pursuing the Ph.D. degree in the Signal Theory and Communications (TSC) Department, within the research group of microwave interaction with living organisms, CommSensLab, UPC. He has held positions at ALCATEL-LUCENT (2013-15), Corporación Nacional de Telecomunicaciones-CNT (2015-15), external researcher at National University of Chimborazo (2018-), and research support technician at the Signal Theory and Communications (TSC) Department, UPC (2020-21). He is currently working on micro-systems design and manufacturing for communication with living organisms and sensing at X-wave frequencies.





**Jordi Romeu** Ph.D., (IEEE Fellow) He received the Ingeniero de Telecomunicación and Doctor Ingeniero de Telecomunicación degrees from the Technical University of Catalonia (UPC) - BarcelonaTech (Spain) in 1986 and 1991, respectively. In 1985, he joined the AntennaLab, Signal Theory and Communications Department (UPC), where he is currently a Full Professor involved in antennas near-field measurements, electromagnetic scattering and imaging, and system miniaturization for wireless and sensing

industrial and bio applications. In 1999, he was a Visiting Scholar at the Antenna Laboratory of the University of California at Los Angeles (USA) on a NATO Scientific Program Scholarship, and at the University of California at Irvine (USA) in 2004. He holds several patents, and has published 60 refereed articles in international journals and 80 conference proceedings. He was a Grand Winner of the European IT Prize, awarded by the European Commission for his contributions in the development of fractal antennas in 1998. He has been involved in the creation of several spin-off companies.



**Luis Jofre-Roca** Ph.D., (IEEE Fellow, 2010) He received the M.Sc. (Ing.) and Ph.D. (Doctor Eng.) degrees in Electronic Engineering (Telecommunication Engineering) from the Technical University of Catalonia (UPC), Barcelona, Spain, in 1978 and 1982, respectively. He has been visiting professor at the Ecole Supérieure d'Electricité Paris (1981-82), with the Georgia Institute of Technology, Atlanta (Fulbright Scholar, 1986-87), and at the University of California, Irvine, CA (2001-02). Director (1989-

94) of the Telecommunication Engineering School, UPC, Vicepresident of the UPC (1994-2000), and General Director and Secretary for Catalan Universities and Research (2011-2016). Director of the Catalan Research Foundation (2002-04), Director of the UPC-Telefonica Chair on Information Society Future Trends (2003-), Principal Investigator of the 2008-13 Spanish Terahertz Sensing Lab Consolider Project, Director of the UPC-SEAT Chair on the Future of Automotive, Research Leader of the 2017-2020 CommSensLab Maria de Maeztu Project, Academic Director of the European Consortium for Future Urban Mobility (Carnet) and Chairman of the EIT-Urban Mobility European Association. He has authored more than 200 scientific and technical papers, reports, and chapters in specialized volumes. Research interests include antennas, electromagnetic scattering and imaging, system miniaturization for wireless and sensing for industrial, scientific and medical applications. Current work focuses on Connected Reconfigurable Autonomous Vehicles for Urban Mobility, Massive MIMO Antennas and Microorganism wireless interaction.